Research Square

Preprints are preliminary reports that have not undergone peer review.
They should not be considered conclusive, used to inform clinical practice,
or referenced by the media as validated information.

Kinetics of degradation of Rhodamine B onto natural and calcined carbon-doped Ca0.5Sr0.5MoO4

Aya El-Shafey
Beni- Suef University
S. I. El-Dek
Beni- Suef University
M. H. Khedr
Beni- Suef University
Nabila Shehata
nabila.shehata@psas.bsu.edu.eg

Beni-Suef University

Research Article

Keywords: photocatalytic degradation, Rhodamine B, natural product, Ca0.5Sr0.5MoO4, kinetics

Posted Date: July 2nd, 2025

DOI: https://doi.org/10.21203/rs.3.rs-6946812/v1

License: This work is licensed under a Creative Commons Attribution 4.0 International License.
Read Full License

Additional Declarations: No competing interests reported.

Kinetics of degradation of Rhodamine B onto natural and calcined carbon-doped $Ca_{0.5}Sr_{0.5}MoO_4$

Aya El-Shafey[a], S. I. El-Dek[a], M.H. Khedr[a], Nabila Shehata[b]

[a] Materials science and nanotechnology department, Faculty of postgraduate studies for advanced sciences, Beni-Suef University, Beni-Suef, Egypt

[b]Environmental Science and Industrial Development Department, Faculty of Postgraduate Studies for Advanced Sciences, Beni-Suef University, Beni-Suef, Egypt. E-mail: nabila.shehata@psas.bsu.edu.eg

Abstract

The problem of water pollution can be treated in more sustainable and environmentally safe ways by developing new catalysts from natural sources. In this work, Naturally Carbon-Doped Strontium Calcium Molybdates was developed by using egg white foam. The catalyst was characterized using several techniques, including FTIR, Diffuse reflectance spectroscopy, Photoluminescence investigations, FE-SEM, EDX, and XRD. The catalyst was thermally activated at 350 ºC and investigated for the removal of Rhodamine B (RhB) from water. The results showed that the removal efficiency of RhB increase with increasing the dose for the catalyst before and after thermal treatment. The optimum pH for the removal of RhB from water is pH 3. The degradation of RhB exceeded 89.6 and 83 % at 20 mgL^{-1} at a dose 0.005 g and pH 3 for the catalyst after and before calcination, respectively. The results suggest the successful development of carbon-doped $Ca_{0.5}Sr_{0.5}MoO_4$ from a sustainable and safer natural source for water remediation purpose.

Keywords: photocatalytic degradation; Rhodamine B; natural product; $Ca_{0.5}Sr_{0.5}MoO_4$; kinetics

1. Introduction

Recently, scientists have turned to innovative solutions to overcome the shortcomings of traditional preparation methods for both physical and chemical methods by using natural resources. These natural or green resources are characterized by many qualities such as availability, sustainability, diversity in properties and types, as well as their low price and low negative impact on the environment, ease of use, and being safe for the health of living organisms, biocompatible and capable of biodegradation [1,2]. In terms of diversity, there are many vital elements used in literature such as plants in their various parts, as well as animal proteins, also biological waste from animal and plant

sources, as well as protozoa, bacteria, fungi, and cell parts of various types [1]. Natural resources are an important and promising trend as a source of materials used in water treatment by photocatalytic degradation methods to get rid of toxic organic pollutants. It is considered a safe, healthy, renewable, and inexpensive source. Due to the nature of natural materials and their differences, they can also be considered multifunctional materials [2–4]. Figure 1a shows the contribution of the applications of bio-based materials in water treatment to the sustainable development goals adopted by the United Nations in 2015. However, there is an increasingly interest on the implementation of biobased nanomaterials in the photocatalytic degradation for wastewater pollutants. It can be seen the increment in the number of publications on the applications of nanomaterials (Figure 1b) and biobased nanomaterials (Figure 1c) in the photodegradation of micropollutants in water bodies.

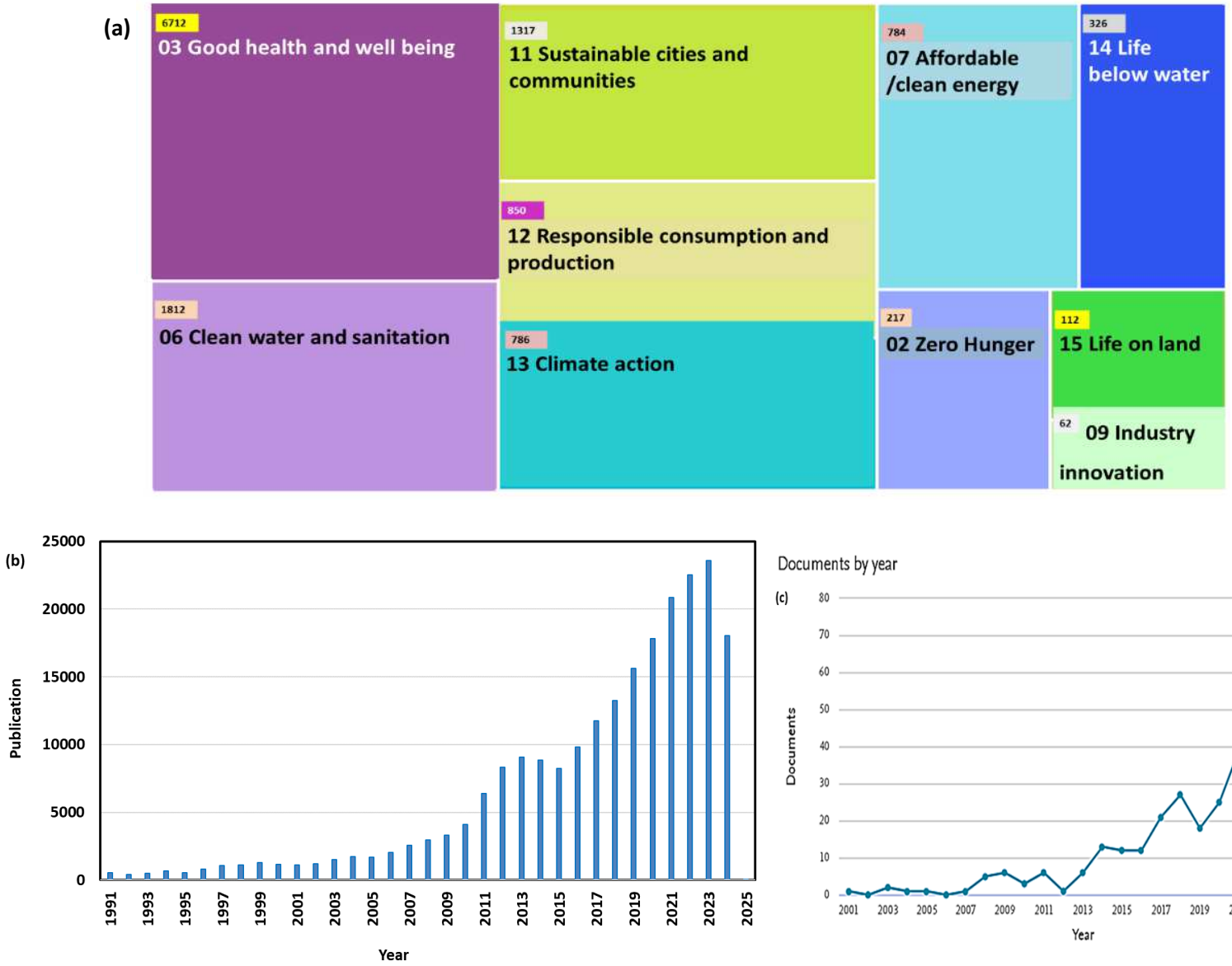
(a)
6712
03 Good health and well being
1317
11 Sustainable cities and communities
784
07 Affordable /clean energy
326
14 Life below water
850
12 Responsible consumption and production
1812
06 Clean water and sanitation
786
13 Climate action
217
02 Zero Hunger
112
15 Life on land
62
09 Industry innovation
(b)
Publication
25000
20000
15000
10000
5000
0
1991
1993
1995
1997
1999
2001
2003
2005
2007
2009
2011
2013
2015
2017
2019
2021
2023
2025
Year
Documents by year
(c)
Documents
80
70
60
50
40
30
20
10
0
2001
2003
2005
2007
2009
2011
2013
2015
2017
2019
2021
2023
2025
Year

Figure

1. The impact of biobased nanomaterials in water treatment on the sustainable development goals according to the Web of Science (a), The number of documents per year on the contribution of green materials (b) in water treatment with special focus photocatalytic degradation per year from SCOPUS (c)

The Scheelite Molybdate ($AMoO_4$, A=Ba, Sr, and Ca) has a tetragonal structure and is classified under the I41/a space group. The intriguing features of molybdates with a scheelite structure have been extensively investigated in recent years due to their diverse replacement possibilities, many compositions, and distinctive structures and properties. The scheelite structures show great potential in several applications, including lasers, photocatalysis, ionic conductor phosphors, and microwave dielectrophoresis [5,6]. To enhance its characteristics, the scheelite structure of the metal molybdate photocatalyst may be modified by adjusting its shape, introducing transition metals or non-metals as dopants, developing a plasmonic or heterojunction structure, and exposing the active facet [7–9]. In addition to its photocatalytic applications, scheelite structures of metal molybdate possess a diverse range of uses in several research domains, such as phosphors, sensors, optical fibers, scintillators, magnets, energy storage, and antibacterial agents. The diverse range of uses of metal molybdates has generated significant interest in several technological fields, such as catalysts and photocatalysis, optics, magnetism, gas sensors, and electrochemistry [10]. The manipulation of dopant ions, their quantity, composition, and the inclusion of vacancies or interstitial positions in the structure allows for precise control over the desired characteristics of scheelite-related materials, thanks to the host lattice's ability to transfer energy. The manipulation of dopant ions in scheelite-related materials allows for precise control over the desired characteristics of these materials. The properties may be effectively modified by adjusting factors such as the quantity of dopant, dopant ratios, and the existence of vacancies or interstitial places in the structure. The latter is significantly impacted by the kind of dopants, the synthesis processes used, and the doping site. Introducing doping in various sublattices, such as Ca/Sr or Mo, and adjusting synthesis parameters, such as temperatures, irradiation duration, pH, and mixing speed, may result in the distortion of MoO_4^{2-} polyhedra. Consequently, this influences the physical and chemical characteristics [6,11,12]. The scheelite-type metal molybdate photocatalyst is distinguished from other metal molybdates. It has a chemical formula of $AMoO_4$ and a tetragonal structure, where A denotes divalent cations. In this structure, divalent metal ions are coordinated with eight oxygen atoms, whereas molybdenum ions are coordinated with four. Superstructures exhibiting a C6 4h point group and I41/a space group may be produced by various configurations using different ordered divalent metals and molybdenum cations. Their energy band gap is within the range of 1.69 to 4.73 eV, which is appropriate [13,14]. Consequently, the structure of the metal molybdate scheelite is formed. Self-assembled hierarchical structures, with distinct forms and unique features, play a crucial role in material synthesis and application. Numbers 2 and 3 provide advantageous functionalities by connecting the nanoscale and microscale realms. Scientists are motivated to construct inorganic hierarchical structures formed by

nanoparticles due to their specific properties. On the other hands, biological elements play an important role in preparing nanomaterials and the role varies from using them as a reducing agent or caping agents or as a stabilizer for materials that prevent aggregation as an auxiliary material in biological reactions or as a source of biocarbon [1,15]. Many types of proteins, including albumin, have been used in the preparation of nanomaterials. What distinguishes albumin is its availability, low price, ease of use, and multiple chemical bonds [16,17]. Subsequently, the aim of this study is to develop green molybdate and investigate the developed materials as a catalyst for rhodamine B dye degradation as a contaminant dye model. The effect of the catalyst dose, solution pH, rhodamine B initial concentration, and contact time on the photocatalytic activity of the catalyst before and after calcination was evaluated. Moreover, the photocatalytic degradation process was evaluated using isotherm and kinetic modeling.

2.1 Materials and Methods

2.1. Preparation of C@$Ca_{0.5}Sr_{0.5}MoO_4$

Solution (A) is prepared by adding 0.4 g of $Ca(NO_3)_2$ to 25 mL of deionized water and stirring for 15 min. Solution (B) with prepared by adding 0.2 g of Sr (nitrate) to 25 mL of deionized water and stirring for 15 min. Solution (C) is prepared by adding 3.3 g Na_2MoO_4 to 100 mL deionized water and stirring for 30 min. The albumin mix is prepared by stirring 5 g from egg albumin for 30 min. Then the solution (C) is mixed dropwise into an albumin mix to develop the solution (D). Solution A and Solution B were mixed dropwise into solution D and stirred for 1 h. the mixture was transferred to a Teflon-lined stainless-steel autoclave and kept in the oven for hydrothermal treatment at 220 °C for 48 h. Finally, the precipitates were collected and washed with a mixture of distilled water and ethanol several times

2.2. Characterization

Powder XRD was recorded using Bruker D8 advance with CuKa (k = 0.15418 nm) radiation to study the phase and crystallite size of the prepared compounds. The analysis held from 4° 2θ to 90° 2θ and a step size is 0.2° with seep 2°/min and 0.1° time /step. SEM micrographs were recorded using HITACHI Model S-3000H to study the size and morphology of the prepared compounds. To study the optical band gap, the UV–Vis diffuse reflectance spectrum was recorded using Shimadzu, a UV-3150 spectrophotometer. The photoluminescence spectrum was recorded using a Hitachi F-7000 luminescence spectrometer at an excitation wavelength of 455 nm to study the luminescence properties and the defects in the prepared compounds. FT-IR spectrum was obtained using a Perkin-Elmer 1650 spectrometer,

with a range of 4000 - 400 cm^{-1}, by measuring KBr pellets. Additionally, FTIR spectra were recorded in the 200 - 1300 cm^{-1} range using an IRAffinity-1S spectrometer.

2.3 Photocatalysis arrays

The efficiency of the developed photocatalyst was assessed by adding 0.005 g of the catalyst into a 20 mL solution of RhB, which had a concentration of 20 parts per million. Subsequently, the process of adsorption and desorption was equilibrated by mixing the mixture completely in the absence of light for 30 min. Subsequently, the RHB solution is used to illuminate and measure any changes in the concentration over a period using a UV spectrophotometer at a wavelength of 553 nm. The removal % is calculated according to Eq. 1:

$$R\% = \frac{C_o - Ct}{C_o} \times 100 \qquad (1)$$

Where C_o and C_t are the initial and concentration of RhB dye at time (t) in mg/L

3. Discussion of the characterization results

Figure 2a displays the XRD patterns of $Ca_{0.5}Sr_{0.5}MoO_4$ for the Albumin mixture in the sample. The patterns exhibit subtle variations in the ICDD number (00-030-1287) with a tetragonal structure and distinct lines that indicate the exceptional crystallinity of the samples. Furthermore, we noticed the absence of any secondary phases. The tetragonal, body-centered crystallite sizes of sample $C@Ca_{0.5}Sr_{0.5}MoO_4$ is 43.46 nm. This is consistent with the XRD sharpness, indicating sample $C@Ca_{0.5}Sr_{0.5}MoO_4$ has larger particles. The diffraction peaks at 18.183°, 27.955°, 30.095°, 33.497°, 45.646°, 48.086°, 51.158°, and 57.784° are corresponding to the lattice planes (101), (112), (004), (200), (204), (220), (116), and (224), respectively. There are variations not only in the peak positions but also in their intensities which reflect the carbon addition Furthermore, there are changes in the strength of several peaks, as well as alterations in the peak widths.

The FT-IR spectrum (Fig. 2b) shows that two bands appear at 3377 cm^{-1}, a wide and medium intensity band, and another very weak band appears at 2921 cm^{-1}. This region is characteristic of O-H. Three bands appear in the region from 1500 cm^{-1} to 2000 cm^{-1}, the strongest of them is wide at 1738 cm^{-1}, which is characteristic of C-C. As for 1387 cm^{-1}, it may indicate the deformation of the bonds Ca-O, Sr-O, Mo-O, Mo-O-Mo (metal oxide band is always below

1000 cm-1) please find a reference to this assignment. The fingerprint region shows 3 bands, one sharp and medium at 412 cm^{-1}, the second sharp and small at 467 cm^{-1}, and the third band appears as a sharp and very strong band, and it is often MoO_4^{-2} illustrates [18].

The SEM analysis (Fig. 2c) revealed the existence of minute particles, as well as a cluster of particles, which were formed by the co-precipitation process. Upon conducting hydrothermal synthesis, we discovered nanoparticles with a spherical shape. The introduction of calcium and strontium atoms resulted in the formation of loosely structured nanoflake particles. The presence of small-sized sheet particles can be attributed to the high-level natural carbon impurity caused by a solid solution of Ca^{2+} and Sr^{-2} cations in the same molybdate. These impurities reduce the potential barrier for the formation of nuclei and growth velocities, resulting in the formation of small, spherical, and well-defined nanocrystals. This is due to the characteristic scheelite structure and the presence of covalent Ca-O and Sr-O bonds, which are both ionic and directional. The elemental mapping indicated that the synthesis approach, which is based on hydrothermal methods, guarantees a uniform distribution of elements on the surface of the particles.

The UV–Vis diffuse reflectance spectrum of $Ca_{0.5}Sr_{0.5}MoO_4$ with albumin were analyzed (Fig. 2d). The optical band gap (E_g) can be determined by using the Kubelka-Munk (K-M) function, which establishes a relationship between absorbance and photon energy (hν) through Eq. 2:

$$(\alpha h\nu)^2 = k(h\nu - E_g) \qquad (2)$$

Here, α represents the absorption coefficient, K is a constant, hν represents discrete photon energy, and E_g represents the band gap energy.

The direct band gap values of the $Ca_{0.5}Sr_{0.5}MoO_4$ with albumin samples were determined to be 4.04 eV, and the indirect band gap equaled 2.5eV. The obtained band gap values are not in agreement with the reported values, possibly due to various factors, including the electronegativity of transition metal ions, connectivity of the polyhedrons, deviation in the O–X–O bonds, distortion of the $[XO_4]^{-2}$ tetrahedrons, growth mechanism, and degree of structural order-disorder in the lattice that gave expectation for add the carbon in the sample and effect in lattice parameter.

The spectra of photoluminescence of $C@Ca_{0.5}Sr_{0.5}MoO_4$ are recorded at room temperature and illustrated in Fig. 2 sharp violet peak is located at about 410 nm, and a blue peak is at about 464 nm. However, we observed lowing in the peak intensity for sample $C@Ca_{0.5}Sr_{0.5}MoO_4$.

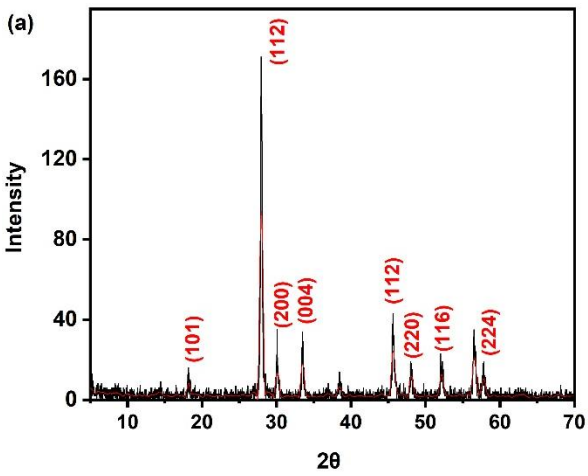
(a)
Intensity
2θ
(101)
(200)
(004)
(112)
(220)
(116)
(224)
(112)

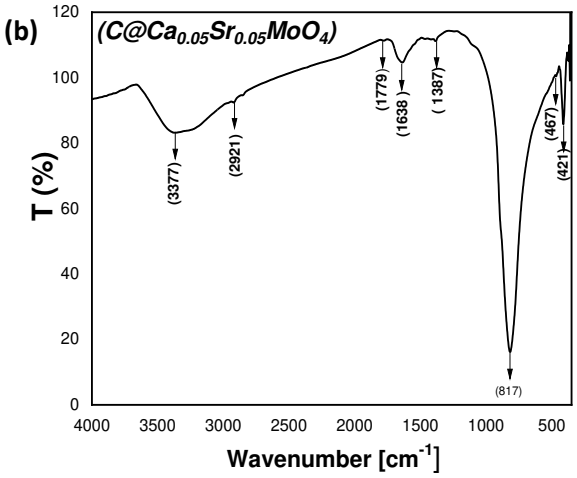
(b)
(C@Ca0.05Sr0.05MoO4)
T (%)
Wavenumber [cm-1]
(3377)
(2921)
(1779)
(1638)
(1387)
(817)
(467)
(421)

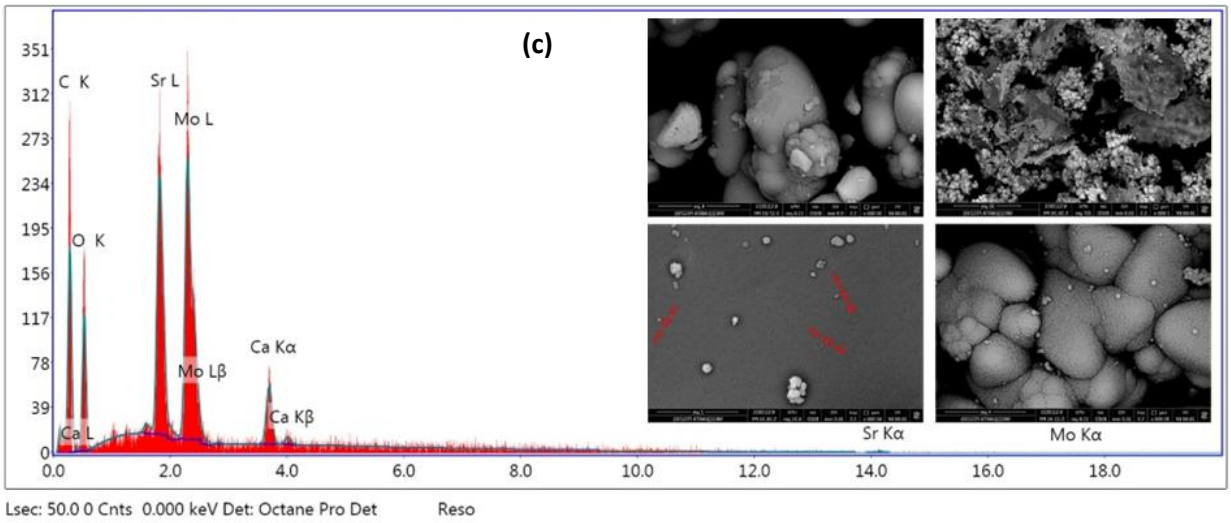
(c)
C K
O K
Ca L
Sr L
Mo L
Mo Lβ
Ca Kα
Ca Kβ
Sr Kα
Mo Kα
Lsec: 50.0 0 Cnts 0.000 keV Det: Octane Pro Det Reso

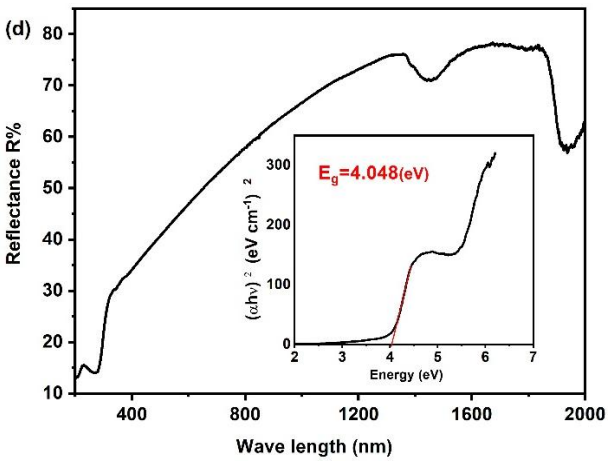
(d)
Reflectance R%
Wave length (nm)
Eg=4.048(eV)
(αhν)2 (eV cm-1)2
Energy (eV)

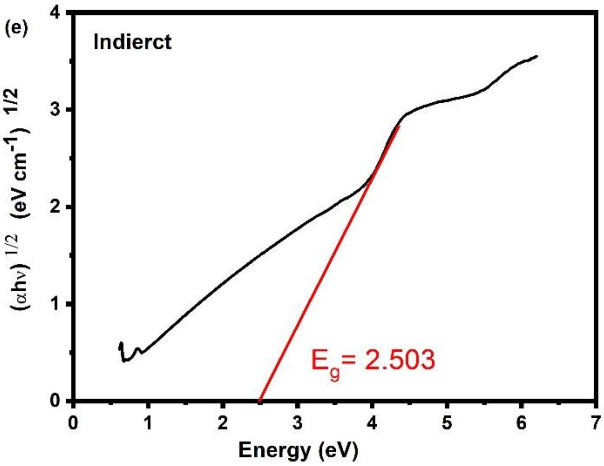
(e)
Indierct
(αhν)1/2 (eV cm-1)1/2
Eg= 2.503
Energy (eV)

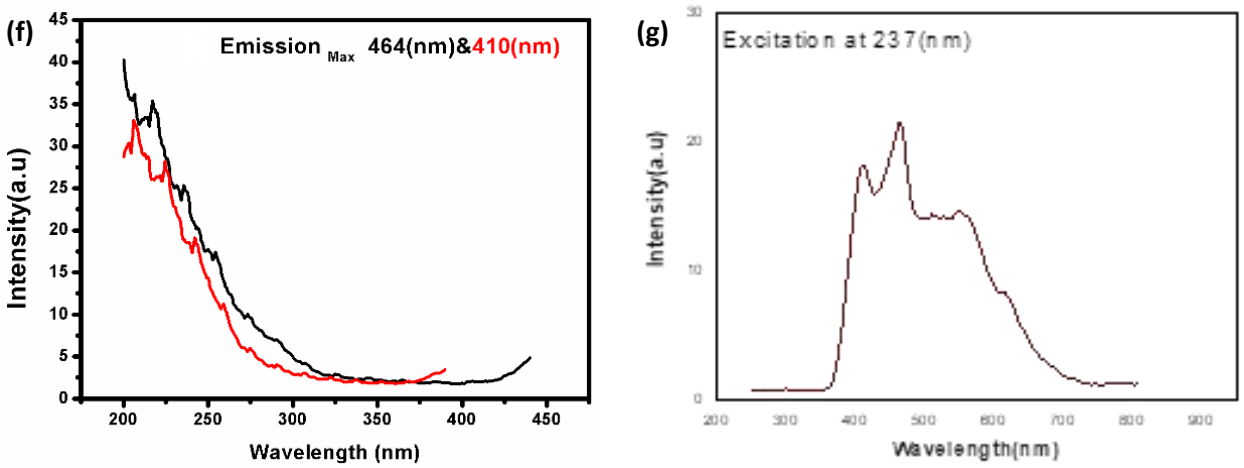

Figure 2. (revise the numeration inside the figure a, b, c, d) correct indirect XRD pattern (a), FTIR spectrum (b) FESEM &EDX (c), Tauc's plot of the optical absorption spectrum (d,e) and PL emission (f) & Excitation spectrum (g) of C@$Ca_{0.5}Sr_{0.5}MoO_4$

4. Assessment of RhB dye photocatalytic degradation

The photocatalytic efficiency was assessed by measuring the degradation of the RhB solution under UV light. The figures present graphs showing the relationship between (C/C_o) and reaction time. C represents the concentration of RhB solution at time t, and C_o is the starting concentration of specimens. The catalyst C@$Ca_{0.5}Sr_{0.5}MoO_4$ exhibits a significant reduction in the photodegradation process of RhB. The enhancement of the degradation process of dye molecules via a photocatalyst is linked to the quantity of electron-hole pairs present on the surface of the photocatalyst. Table 1 shows a comparison of the photocatalytic degradation of Rhodamine B using different sorbents.

Table 1. A comparative analysis of the removal of RhB from water using another catalyst in the literature.

Sorbent	Photocatalytic degradation (%)	Dose (g)	pH	Equilibrium time (min)	Reference
$CuBi_2O_4/Bi_2MoO_6$ heterojunction	96.97	0.02	-	30	[19]
$Sr_{(1-3)x}Bi_2 x \Phi x MoO_4^-$	92.7 92.7	0.2	Acidic	30	[20]

$Ag/Ag_2MoO_4/BiOI$ - Heterojunction	99.4	0.1	-	50	[21]
Ag/Bi_2MoO_6	100	0.2	-	150	[22]
Ag_2MoO_4	95	0.05	-	60	[23]
$C@Ca_{(0.5)}Sr_{(0.5)}MoO_4$	83	0.005 0.001 0.003	3, 5.7	30	This study

4.1 Impact of time

The degradation performance of $C@Ca_{0.5}Sr_{0.5}MoO_4$ before (Fig. 3a) and after (Fig. 3b) thermal treatment for three doses (0.001, 0.003 and 0.005) with times shows that the activity of $C@Ca_{0.5}Sr_{0.5}MoO_4$ achieved a degradation 73%, 76% and 76% respectively at 30 min and after thermal treatment, these values are decreased to 23%, 30% and 37% at 30 min, respectively. This suggesting that $C@Ca_{0.5}Sr_{0.5}MoO_4$ have higher photocatalytic activity than after thermal treatment for all doses under study. Also, the results show that increasing the doses has a significant effect on the decomposition rate where the highest degradation rate follows the order 0.005 > 0.003 > 0.001 g for the developing catalyst before and after thermal treatment and this is attributed to the increase in the available active cites of the catalyst with the increment of catalyst mass.

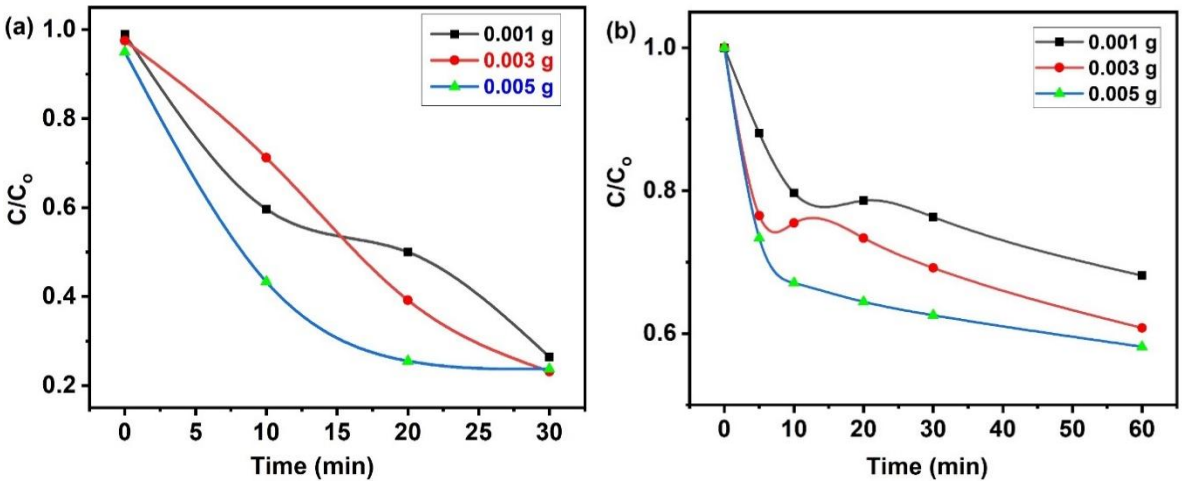

Figure 3. Effect of dose on concentration reduction efficiency of RhB with varied time at pH 7 for C@$Ca_{0.5}Sr_{0.5}MoO_4$ (a) and calcined $Ca_{0.5}Sr_{0.5}MoO_4$/C at 350˚C (b)

4.2 Impact of pH and time

Figure 4 shows the impact of pH and time on the percentage of degradation of RhB. It was found that pH 3 is the optimum for the materials before and after treatment. Figure 4(a) shows that the degradation % of RhB using C@$Ca_{0.5}Sr_{0.5}MoO_4$ at different pH (3, 5& 8) reach 83%,20%, and 16% at 30 min, and for C@$Ca_{0.5}Sr_{0.5}MoO_4$ at 350˚C (Fig. 4b), it reaches 89.6%, 28%, and 21%% at 30 min. The degradation performance is high at acidic conditions that result agree with Eh-pH diagram of $[MoO_4]^{-2}$ that $[MoO_4]^{-2}$ worked ideal at pH 3 and pH 7 (Atlas of Eh-PH Diagrams Intercomparison of Thermodynamic Databases.(2005) in addition to the cationic nature of RhB dye [24], so the media in pH 3 improves the electrostatic interactions between the sorbent and dye. However, the photocatalytic degradation of RhB at pH 3 is much improved after calcination. This suggests that the pH of the solution has a significant effect on the overall performance of the catalyst.

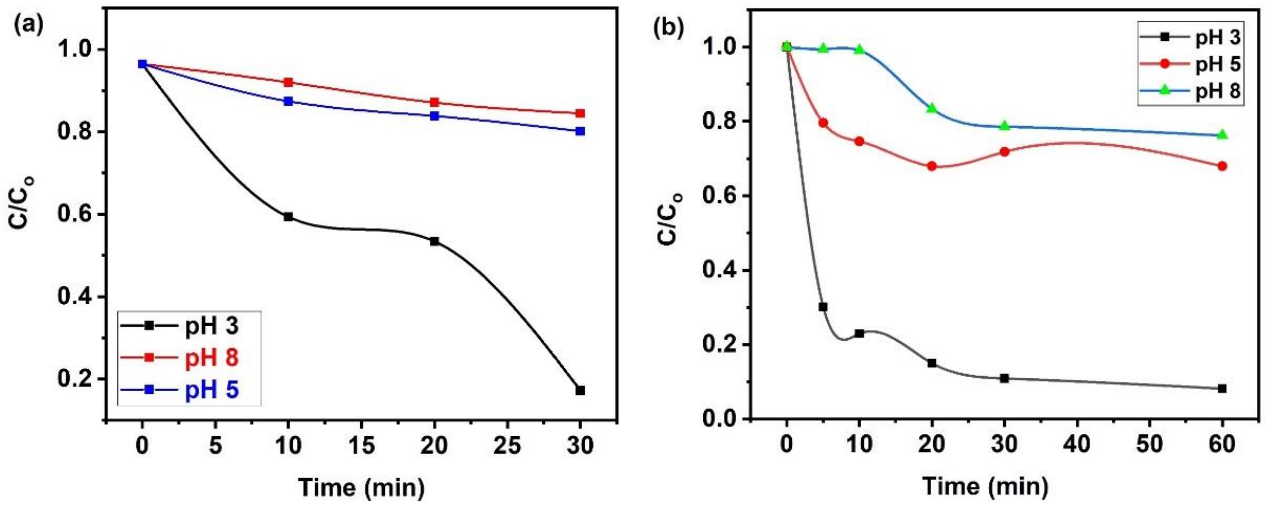

Figure 4. Effect of different pH on concentration reduction efficiency of RhB with time for C@$Ca_{0.5}Sr_{0.5}MoO_4$ (a) and calcined C@$Ca_{0.5}Sr_{0.5}MoO_4$ (b)

4.3 Photocatalytic degradation modelling

Table 2 shows the coefficients obtained from the isothermal Langmuir and Freundlich equations (linear and nonlinear) for the photocatalytic degradation of RhB onto C@$Ca_{0.5}Sr_{0.5}MoO_4$ and C@$Ca_{0.5}Sr_{0.5}MoO_4$@350˚C. The obtained values revealed that both samples follow the linear Langmuir model.

Table 2 Langmuir and Freundlich isotherm (linear and nonlinear) for RhB removal at C@$Ca_{0.5}Sr_{0.5}MoO_4$ and C@$Ca_{0.5}Sr_{0.5}MoO_4$ /350˚ C

Model		**Parameter**	**C@$Ca_{0.5}Sr_{0.5}MoO_4$**	**C@$Ca_{0.5}Sr_{0.5}MoO_4$/350 ˚C**
Langmuir	Nonlinear	q_{max} (mgg^{-1})	4707.52	828.62
		K_L (Lmg^{-1})	0.0025	0.1895
		R^2	0.541	0.123
	Linear	q_{max} (mgg^{-1})	34.25	178.57
		K_L (Lmg^{-1})	5.31	56
		R^2	0.95	0.927
Freundlich	Nonlinear	k_F (Lmg^{-1})	1.078	0.953
		1/n	11.34	125.65
		R^2	0.5422	0.1242
	Linear	k_F (Lmg^{-1})	12.59	52.83
		1/n	3.209	0.796
		R^2	0.401	0.125

Where the calculated values of q_{max} are close to the experimental one along with high R^2 values (0.95 and 0.927 for C@$Ca_{0.5}Sr_{0.5}MoO_4$ and C@$Ca_{0.5}Sr_{0.5}MoO_4$@350˚C, respectively). In contrast to the non-linear Langmuir model, where the calculated values of q_{max} are much higher than the experimental one in addition to low R^2 values (0.451 and 0.123 for C@$Ca_{0.5}Sr_{0.5}MoO_4$ and C@$Ca_{0.5}Sr_{0.5}MoO_4$@350˚C, respectively). For Freundlich models, both of linear and non-linear forms failed to describe the degradation of RhB onto both of C@$Ca_{0.5}Sr_{0.5}MoO_4$ and C@$Ca_{0.5}Sr_{0.5}MoO_4$@350˚C, respectively where the values of R^2 are low (0.124- 0.542).

5. Kinetics Study

The photocatalytic process of RhB using C@$Ca_{0.5}Sr_{0.5}MoO_4$ was analyzed using 5 kinetic models; Pseudo-first order (Eq. 3), pseudo-second-order (Eq. 4), mixed order 1,2 order (Eq. 5), Avrami (Eq. 6), and intra-particle diffusion (Eq. 7), models as follows:

$$q_t = q_e\,(1 - \exp(-k_1 t)) \quad (3)$$

$$q_t = \frac{k_2 q_e^2 t}{1 + k_2 q_e t} \quad (4)$$

$$q_t = q_e\,\frac{1-\exp(-kt)}{1-f_2\exp(-kt)} \quad (5)$$

$$q_t = q_e\,[1 - \exp(-k_{av}t)n_{av}] \quad (6)$$

$$q_t = k_{ip}\sqrt{t} + c_{ip} \quad (7)$$

5.1 Effect of pH and time

Fig 5(a) and Table 3 combine the results of the fitting of PFO, PSO, MFSO, Avrami, and IPD models for the photocatalytic degradation of RhB onto C@$Ca_{0.5}Sr_{0.5}MoO_4$ at pH 3. The IPD model is the best to describe the photocatalytic degradation kinetics of RhB onto C@$Ca_{0.5}Sr_{0.5}MoO_4$ since the calculated values are agreed with the experimental one and the value of R^2 is high (0.909). Although all the models yield correlation coefficients (R^2) are high as 0.937, 0.935, 0.9377, and 0.937 for PFO, PSO, MFSO, and Avrami models, respectively; However, the models are not suitable for the photocatalytic degradation system under study since the calculated values of q_{max} are much higher than the experimental one. For pH 5 (Fig 5b), still the IPD model is predominant with R^2 0.97. Also, PFO, and Avrami models fit the experimental values of RhB degradation onto C@$Ca_{0.5}Sr_{0.5}MoO_4$ accurately with values very high as 0.990, and 0.994, respectively. Also, the calculated values of q_{max} are close to the experimental one. on the other hands, PSO and MFSO are not accurate for this photocatalytic degradation system since the predicted values according to these models are higher than the experimental one. Similar to the results of pH 3, only IPD model can describe the degradation of RhB onto C@$Ca_{0.5}Sr_{0.5}MoO_4$ at pH 8 (Fig 5c) since the calculated values are closed to the experimental one and R^2 values are high as 0.945 while the other models failed to predict the experimental q_{max} even with the high correlation coefficient related to these models (Table 3).

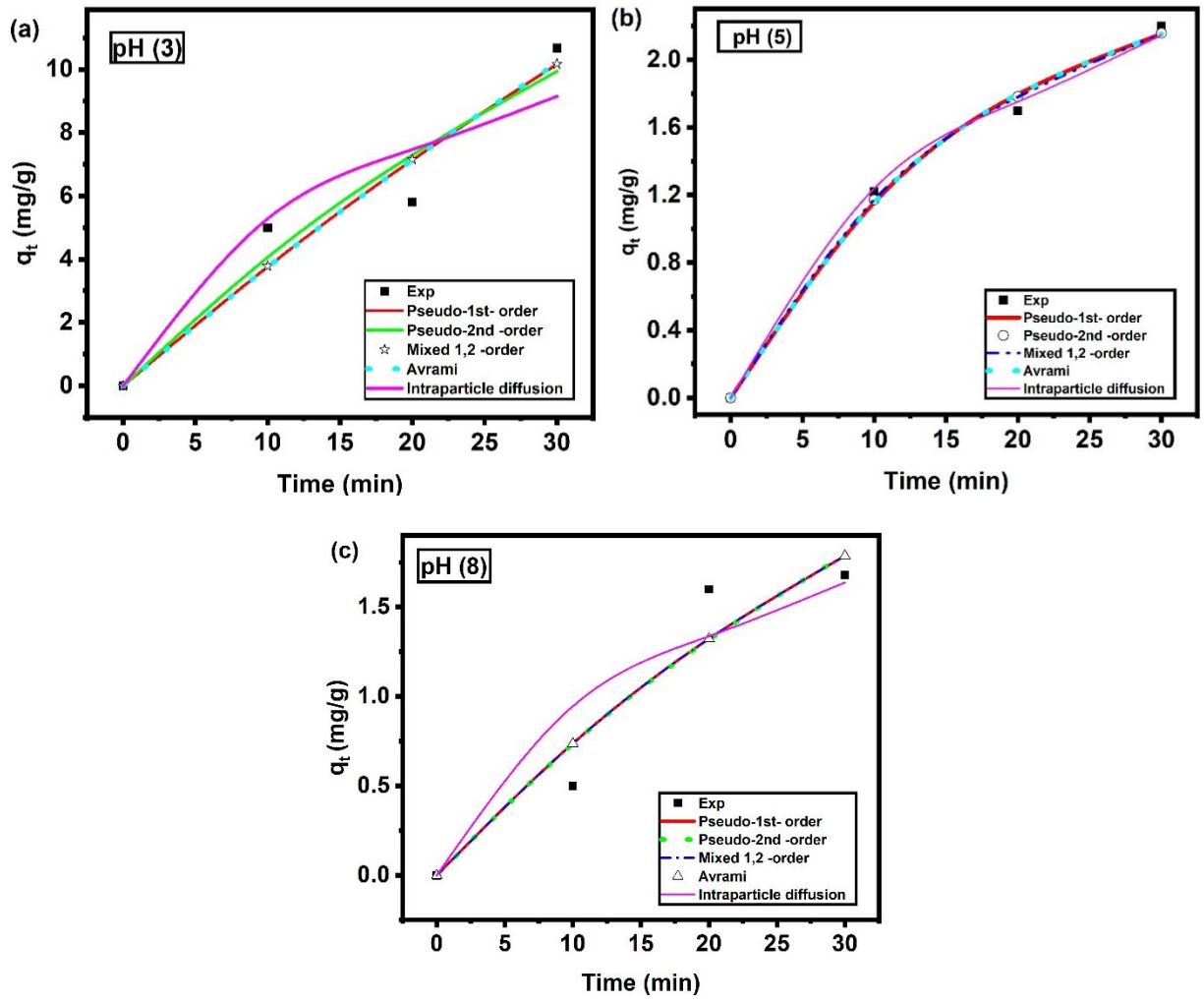

Figure 5. Kinetic results of the fitting of PFO, PSO, MFSO, IPD, and Avrami models for the photocatalytic degradation of RhB onto C@$Ca_{0.5}Sr_{0.5}MoO_4$ at pH 3 (a), 5 (b), and 8 (c)

Figure 6 and Table 3 combine the results of the fitting of PFO, PSO, MFSO, Avrami, and IPD models for the photocatalytic degradation of RhB onto C@$Ca_{0.5}Sr_{0.5}MoO_4$ after thermal treatment at pH 3. PFO and Avrami models can accurately describe the photocatalytic degradation system at pH 3 (Fig. 6a) where the calculated values are very close to the experimental values of q_{max} in addition to high values of R^2 (Table 2). Although PSO and MFSO models showed high values of R^2 (0.999 and 0.998, respectively); However, the calculated values of q_{max} according to these models are slightly higher than the experimental one. On the other hand, IPD failed to describe the photocatalytic degradation system at pH 3 where there is no agreement between the calculated and the experimental values of q_{max}

in addition to a low value of R^2 (0.702). For pH 5 (Fig. 6b), PFO, PSO, MFSO and Avrami models can describe the photocatalytic degradation system with R^2 values as high as 0.982, 0.981, 0.981, and 0.982, respectively. Similar to the results at pH 3, the IPD model is not suitable for this photocatalytic degradation system. For pH 8 (Fig. 6c), none of PFO, PSO, MFSO, and Avrami models can describe the photocatalytic degradation of RhB onto the catalyst after thermal treatment where the predicted values of q_{max} are higher than the experimental one in addition to low values of R^2 (0.860-0.868). Moreover, IPD is not suitable for this system where R^2 is low (0.770)

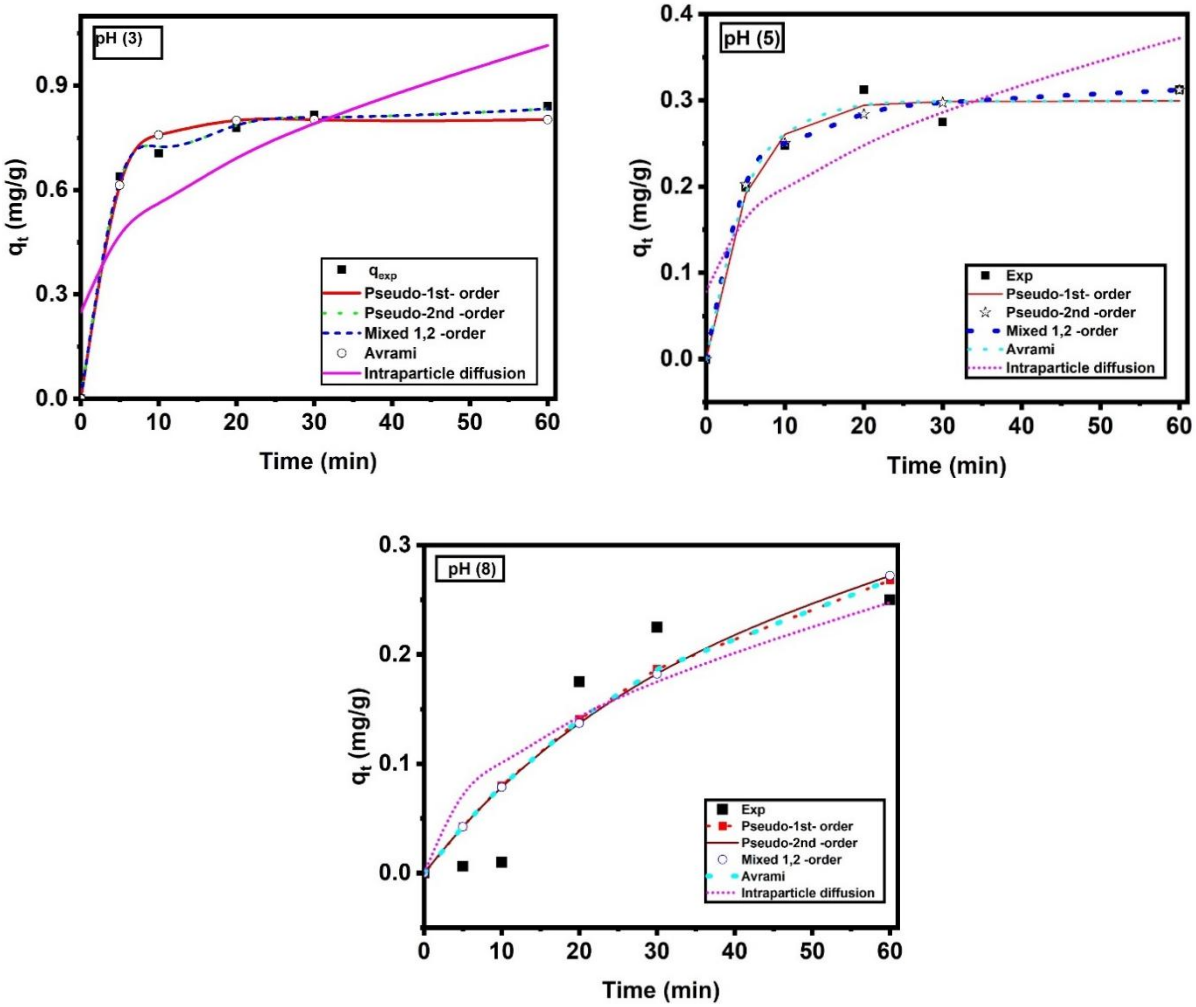

Figure 6. Kinetic results of the fitting of PFO, PSO, MFSO, IPD and Avrami models for the photocatalytic degradation of RhB onto $C@Ca_{0.5}Sr_{0.5}MoO_4$/350˚C at pH 5(a), 3(b) and 8(c)

Table 3. The parameters for PFO, PSO, MFSO, Avrami, and IPD models for the photocatalytic degradation of RHB onto $C@Ca_{0.5}Sr_{0.5}MoO_4$ at pH 3, 5 and 8

		C@$Ca_{0.5}Sr_{0.5}MoO_4$			C@$Ca_{0.5}Sr_{0.5}MoO_4$/350 ºC		
Model	**Parameter**	**pH 3**	**pH 5**	**pH 8**	**pH 3**	**pH 5**	**pH 8**
PFO	K_1 [min^{-1}]	0.010	0.058	0.019	0.289	0.204	0.028
$q_t = q_e\ (1 -$	q_e [mgg^{-1}]	36.9	2.60	3.65	0.803	0.299	0.330
$\exp(-k_1 t))$	R^2 [-]	0.937	0.99	0.99	0.989	0.982	0.868
PSO	K_2 [$gmg^{-1}.min$]	0.0003	0.012	0.0016	0.629	0.979	0.032
$q_t = \frac{k_2 q_e^2 t}{1+k_2 q_e t}$	q_e [mgg^{-1}]	36.01	3.72	6.67	0.859	0.328	0.536
	R^2 [-]	0.935	0.9958	0.994	0.999	0.981	0.860
MFSO	K [$mg.g^{-1}.\ min^{-1}$]	0.0028	0.008	0.019	0.0045	0.0008	4.1E-05
$q_t = q_e$	q_e [mgg^{-1}]	53.24	3.40	3.638	0.8553	0.328	0.536
$\frac{1-\exp(-kt)}{1-f_2 exp\ (-kt)}$	f_2 [-]	0.617	0.82	0	0	0.9976	0.9976
	R^2 [-]	0.938	0.996	0.995	0.998	0.981	0.860
Avrami	q_e [mgg^{-1}]	39.161	2.60	3.64	0.803	0.299	0.330
$q_t = q_e$ [1 - exp(-	k_{av} [min^{-1}]	0.103	0.249	0.145	0.538	2.022	0.151
$k_{av}t)^{nav}$]	n_{av} [-]	0.0975	0.235	0.137	0.538	0.101	0.184
	R^2 [-]	0.937	0.994	0.995	0.989	0.982	0.868
IPD	k_{ip} [$mgg^{-1}.min^{1/2}$]	1.67	0.39	0.27	0.099	0.038	0.032
$q_t = k_{ip}\sqrt{t}+c_{ip}$	c_{ip} [mgg^{-1}]	0	0	0	0.249	0.079	0
	R^2 [-]	0.909	0.997	0.945	0.702	0.746	0.770

In the photocatalytic degradation of RhB onto C@$Ca_{0.5}Sr_{0.5}MoO_4$, the kinetic results showed that the IPD model is the predominant models under all pH values under study while for C@$Ca_{0.5}Sr_{0.5}MoO_4$/350 ºC, PFO and Avrami models were the best to describe the photocatalytic degradation of RhB at pH 3 and PFO, PSO, MFSO and Avrami models were more appropriate for the photocatalytic degradation of RhB at pH 5. For pH 8, none of the models was able to fit the experimental data. This confirms that the pH of the dye plays a considerable role in kinetic of the RhB degradation onto C@$Ca_{0.5}Sr_{0.5}MoO_4$/350 ºC.

5.2 Effect of dose and time

The fitting of PFO, PSO, MFSO, IPD, and Avrami's photocatalytic degradation kinetic modeling to the experimental data for RhB photocatalytic degradation onto 0.001 g from $Ca_{0.5}Sr_{0.5}MoO_4$ is depicted in Figure 7(a). The IPD model is the best to describe the photocatalytic degradation system where the calculated values agree with the experimental one in addition to the high value of R^2 (0.976). Although the high values of R^2 (PFO (0.969), PSO (0.973), MFSO (0.972), and Avrami (0.970)), the calculated values according to PFO, PSO, MFSO and Avrami are higher than the experimental one. For dose 0.003 g (Fig. 7b), similar results were recorded where PFO, PSO, MFSO, and Avrami models don't fit the experimental data accurately and the calculated values according to these models are higher than the experimental one even with the high correlation coefficients associated with these models. Only the IPD model can fit the data well with $R^2 = 0.934$. For dose, 0.005 g (Fig. 7c), different kinetic performance is recorded and PFO and Avrami models can fit the data well with R^2 0.998 for both models; however, PSO and MFSO models can't accurately describe the photocatalytic degradation of RhB at dose 0.005 g since the predicted q_{max} values according to these models are higher than the experimental one. On the other hand, the IPD model is not suitable for this system since there is no agreement between the calculated and the experimental values of q_{max} even with the high values of R^2 (Table 4).

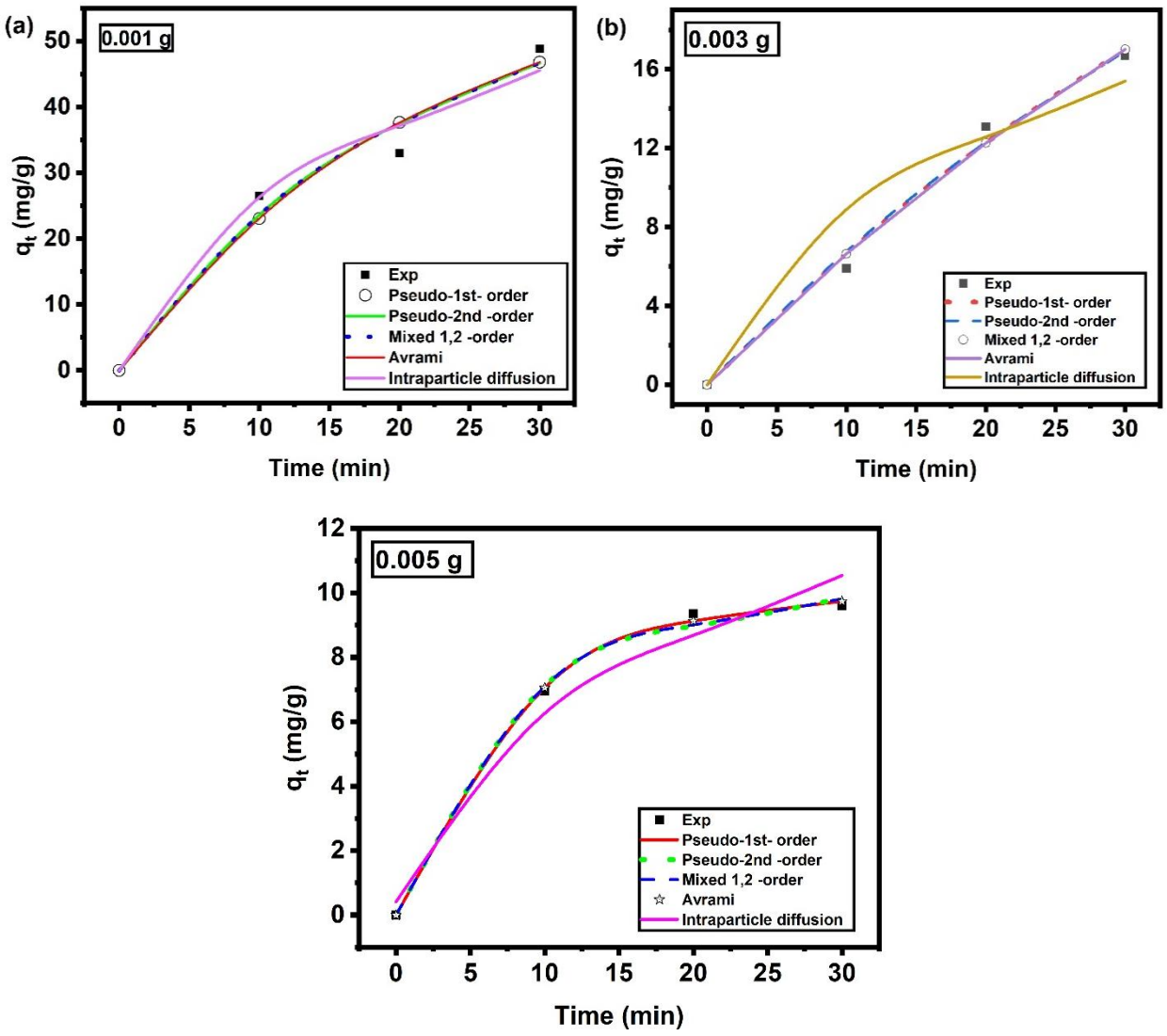

Figure 7. Kinetic results of the fitting of PFO, PSO, MFSO, IPD, and Avrami models for the photocatalytic degradation of RhB onto C@$Ca_{0.5}Sr_{0.5}MoO_4$ at adsorbent mass 0.001 (a), 0.033 (b) and 0.005 (c) g

The kinetic results of the fitting of PFO, PSO, MFSO, IPD, and Avrami models for the photocatalytic degradation of RhB onto C@$Ca_{0.5}Sr_{0.5}MoO_4$ after calcination at catalyst mass 0.001 (Fig. 8a), 0.003 (Fig. 8b) and 0.005 (Fig. 8c) g show that for dose 0.001 g, only IPD model can describe the photocatalytic degradation system with high R^2 (0.939), Although the other models yield high correlation coefficients; 0.934, 0.964, 0.964 and 0.934 for PFO, PSO, MFSO and Avrami, respectively; however, the calculated values according to these models are higher than the experimental one (Table 4). For doses, 0.003 and 0.005 g, the kinetic performance is similar where both PSO and MFSO models can fit the data accurately with high R^2 values (0.938-0.995). PFO and Avrami models don't accurately fit the

experimental data for both doses even at the high correlation coefficients reported (Table 4). On the other hand, IPD model is not suitable for both systems.

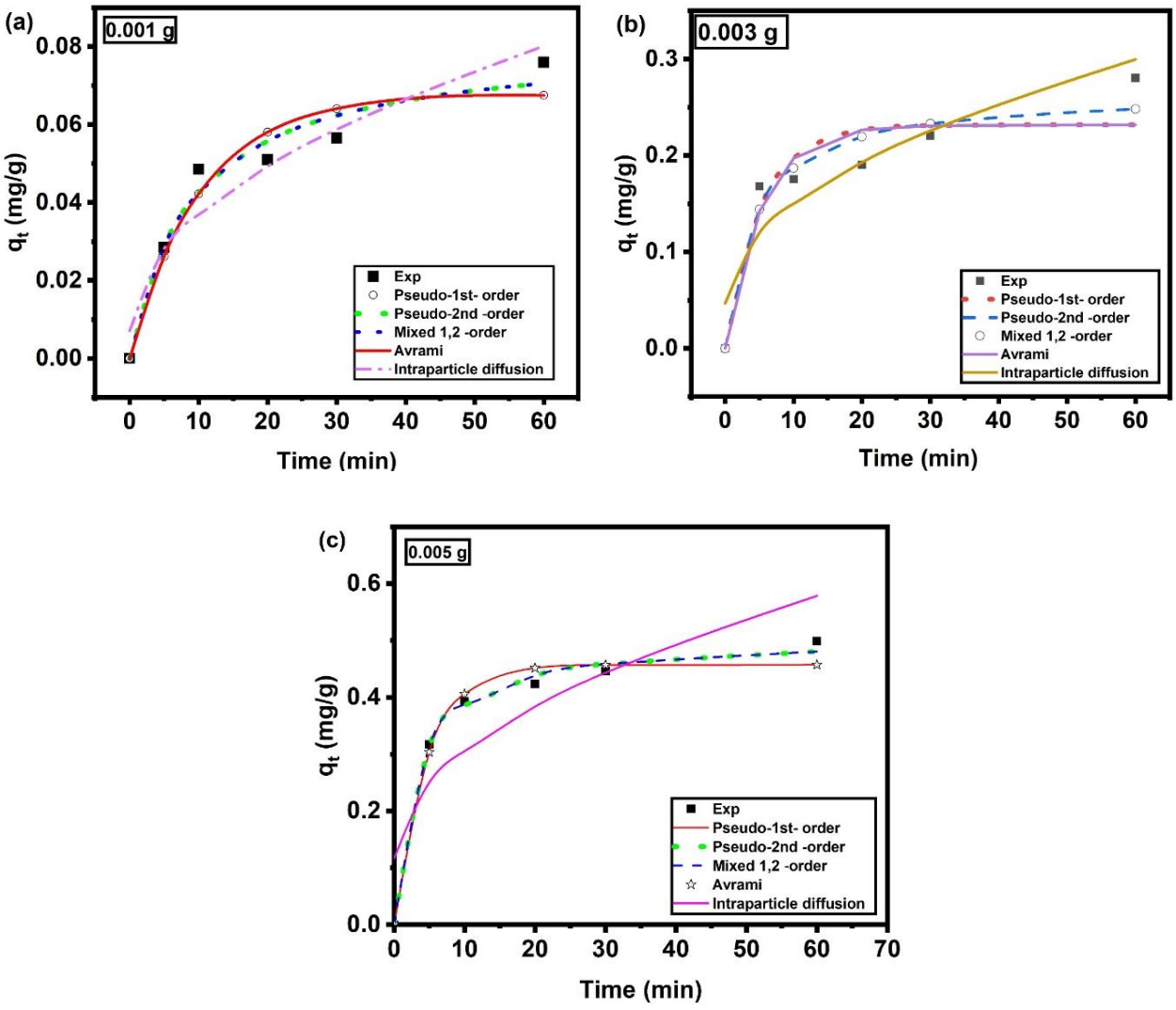

Figure 8. kinetic results of the fitting of PFO, PSO, MFSO, IPD, and Avrami models for the photocatalytic degradation of RhB onto ($Ca_{0.5}Sr_{0.5}MoO_4$/C at 350 ˚C) adsorbent mass 0.001 (a), 0.003 (b) and 0.005 (c) g

Table 4. The parameters for PFO, PSO, MFSO, Avrami, and IPD models for the photocatalytic degradation of RhB onto C@$Ca_{0.5}Sr_{0.5}MoO_4$ before and after calcination at dose 0.001, 0.003 and 0.005 g

		$C@Ca_{0.5}Sr_{0.5}MoO_4$			$C@Ca_{0.5}Sr_{0.5}MoO_4$/350 ºC		
Model	**Parameter**	**Mass (g)**			**Mass (g)**		
	q_{exp} [mgg^{-1}]	**0.005**	**0.003**	**0.001**	**0.005**	**0.003**	**0.001**
PFO	K_1 [min^{-1}]	0.122	0.0168	0.0461	0.218	0.190	0.098
$q_t = q_e (1 -$	q_e [mgg^{-1}]	9.998	42.90	62.499	0.458	0.232	0.068
$\exp(-k_1 t))$	R^2 [-]	0.998	0.991	0.969	0.982	0.888	0.934
PSO	K_2 [$gmg^{-1}.min$]	0.012	0.0001	0.0003	0.649	0.889	1.339
$q_t = \frac{k_2 q_e^2 t}{1+k_2 q_e t}$	q_e [mgg^{-1}]	12.171	68.631	91.41	0.505	0.266	0.081
	R^2 [-]	0.996	0.9915	0.973	0.995	0.938	0.964
MFSO	K [$mgg^{-1}.min^{-1}$]	0.053	0.0168	0.0020	0.0003	0.0008	0.0007
$q_t = q_e$	q_e [mgg^{-1}]	10.69	42.81	88.33	0.505	0.265	0.081
$\frac{1-\exp(-kt)}{1-f_2 exp\ (-kt)}$	f_2 [-]	0.642	0	0.94	0.999	0.997	0.994
	R^2 [-]	0.996	0.991	0.972	0.995	0.938	0.964
Avrami	q_e [mgg^{-1}]	9.997	42.806	62.49	0.457	0.232	0.068
$q_t = q_e [1 - \exp(-$	k_{av} [min^{-1}]	0.3598	0.134	0.221	0.381	1.132	0.221
$k_{av}t)n_{av}]$	n_{av} [-]	0.340	0.1263	0.2087	0.572	0.168	0.442
	R^2 [-]	0.998	0.99	0.97	0.982	0.888	0.934
IPD	k_{ip} [$mgg^{-1}.min^{1/2}$]	1.85	2.81	8.3	0.059	0.033	0.009
$qt = k_{ip} \sqrt{t} + c_{ip}$	c_{ip} [mgg^{-1}]	0.416	0	0	0.117	0.047	0.007
	R^2 [-]	0.983	0.934	0.976	0.792	0.874	0.939

For the impact of the catalyst does, it can be concluded that increasing the dose from 0.001 to 0.003 g, changes the kinetic modelling of the decomposition of Rhodamine B dye onto C@$Ca_{0.5}Sr_{0.5}MoO_4$ from IPD to PFO and Avrami models. For C@$Ca_{0.5}Sr_{0.5}MoO_4$/350 ºC, the kinetic modelling is altered from IPD at dose 0.001 g to PSO and MFSO

models at doses 0.003 and 0.005 g. This is suggesting that the kinetic modelling for the photocatalytic degradation of RhB onto the photocatalyst before and after calcination is sensitive to the dose of the catalyst.

Conclusion

This study investigated the development and characterization of C@$Ca_{0.5}Sr_{0.5}MoO_4$, as well as the kinetic behavior of the decomposition of RhB dye onto C@$Ca_{0.5}Sr_{0.5}MoO_4$ before and after calcination. The results showed that the intraparticle diffusion model is the best to describe the degradation of RhB onto C@$Ca_{0.5}Sr_{0.5}MoO_4$ at different pH (3,5, and 8). On the other hands, the intraparticle diffusion model fail to describe the degradation of RhB onto C@$Ca_{0.5}Sr_{0.5}MoO_4$ after thermal treatment and the kinetic performance of the dye onto the catalyst after the thermal treatment is significantly affected by the change in pH and catalyst dose. The photocatalytic degradation isotherm modelling showed that the linear form of Langmuir model is the best to describe the photodegradation of RhB onto C@$Ca_{0.5}Sr_{0.5}MoO_4$ and C@$Ca_{0.5}Sr_{0.5}MoO_4$/350 ºC

Declaration:

The authors declare that they have no known competing personal relationships or financial interests that could have appeared to influence the work reported in this article.

Data availability

Data will be made available on request.

Acknowledgment

Glory be to You! We have no knowledge except what You have taught us. You are truly the All-Knowing, All-Wise (Quran.2-32)

Funding

Open access funding provided by The Science, Technology & Innovation Funding Authority (STDF) in cooperation with The Egyptian Knowledge Bank (EKB).

Author information

Authors and Affiliations

Materials science and nanotechnology department, Faculty of postgraduate studies for advanced sciences, Beni-Suef University, Beni-Suef, Egypt

Aya El-Shafey, S. I. El-Dek, M.H. Khedr

Environmental Science and Industrial Development Department, Faculty of Postgraduate Studies for Advanced Sciences, Beni-Suef University, Beni-Suef, Egypt

Nabila Shehata

Corresponding author

Correspondence to Nabila Shehata

Contributions

S. I. El, M.H. Kh supervised the work, A El performed the literture survey, data analysis, drafting of the work and revision, S. I. El, M.H. Kh, and N Sh contributed to writing-reviewing and editing the final version of the manuscript

Ethics declarations

Ethics approval and consent to participate

This article does not contain any studies with human participants or animals performed by any of the authors.

Consent for publication

Not applicable.

Competing interests

It is hereby declared that all the authors have read and approved the manuscript and there is no conflict of interest.

References

1. Ashrafi G, Nasrollahzadeh M, Jaleh B, Sajjadi M, Ghafuri H. Biowaste-and nature-derived (nano) materials: Biosynthesis, stability and environmental applications. Adv Colloid Interface Sci. 2022;301:102599.

2. Osman AI, Zhang Y, Farghali M, Rashwan AK, Eltaweil AS, Abd El-Monaem EM, et al. Synthesis of green nanoparticles for energy, biomedical, environmental, agricultural, and food applications: A review. Environ Chem Lett. 2024;22:841–87.

3. He Q, He D, Zhang Y, Luo X, Hu L, Jiang P. Mo2C and its composites derived from egg white for hydrogen evolution reaction at all pH range. ChemistrySelect. 2018;3:4683–6.

4. Ying S, Guan Z, Ofoegbu PC, Clubb P, Rico C, He F, et al. Green synthesis of nanoparticles: Current

developments and limitations. Environ Technol Innov. 2022;26:102336.

5. Li F, Xie H, Xi H, Dang F, Wang X. Luminescent properties of sol–gel processed red-emitting phosphor Ca0. 6Sr0. 4–1.5 x-0.5 yMo0. 4 W0. 6O4: EuxLiy. Luminescence. 2015;30:600–4.

6. Mikhaylovskaya ZA, Buyanova ES, Petrova SA, Nikitina AA. Sheelite-related strontium molybdates: synthesis and characterization. Chim Techno Acta 2018 Vol 5№ 4. 2018;5:189–95.

7. Ramarao SD, Kiran SR, Murthy VRK. Structural, lattice vibrational, optical and microwave dielectric studies on Ca1− xSrxMoO4 ceramics with scheelite structure. Mater Res Bull. 2014;56:71–9.

8. Bharat LK, Raju GSR, Yu JS. Red and green colors emitting spherical-shaped calcium molybdate nanophosphors for enhanced latent fingerprint detection. Sci Rep. 2017;7:11571.

9. Gaidamavičienė G, Žalga A. Synthesis, a structural and thermoanalytical study of Ca1-xSrxMoO4 ceramic. Mater Chem Phys. 2020;241:122339.

10. Vidya S, John A, Solomon S, Thomas JK. Optical and dielectric properties of SrMoO4 powders prepared by the combustion synthesis method. Adv Mater Res. 2012;1:191.

11. Tiwari A. Advancement of Materials to Sustainable & Green World. Adv Mater Lett [Internet]. 2023;14:1724–2303. Available from: https://aml.iaamonline.org/article_23878.html

12. Ribeiro F de AS, da Silva Junior MM, Duarte CR, da Silva RC, de Sousa Marques V. Síntese de cristais de Ca (0, 5) Sr (0, 5) MoO4 via método de coprecipitação e processamento em forno micro-ondas hidrotermal: estudo estrutural e fotoluminescente. Res Soc Dev. 2020;9:e679119592–e679119592.

13. Huerta-Flores AM, Juárez-Ramírez I, Torres-Martínez LM, Carrera-Crespo JE, Gómez-Bustamante T, Sarabia-Ramos O. Synthesis of AMoO4 (A= Ca, Sr, Ba) photocatalysts and their potential application for hydrogen evolution and the degradation of tetracycline in water. J Photochem Photobiol A Chem. 2018;356:29–37.

14. Mikhaylovskaya ZA, Buyanova ES, Petrova SA, Klimova A V. ABO4 type scheelite phases in (Ca/Sr) MoO4-BiVO4-Bi2Mo3O12 systems: synthesis, structure and optical properties. Chim Techno Acta 2021 Vol 8№ 2. 2021;8.

15. Karunakaran G, Sudha KG, Ali S, Cho E-B. Biosynthesis of nanoparticles from various biological sources and its biomedical applications. Molecules. 2023;28:4527.

16. Vijayakumar TS, Mahboob S, Bupesh G, Vasanth S, Al-Ghanim KA, Al-Misned F, et al. Facile synthesis and biophysical characterization of egg albumen-wrapped zinc oxide nanoparticles: A potential drug delivery vehicles

for anticancer therapy. J Drug Deliv Sci Technol. 2020;60:102015.

17. Cardoso-Ávila PE, Pichardo-Molina JL, Vázquez-Olmos M, González-Aguiñaga E. Chicken egg white as a "greener" biomass source for the rapid synthesis of fluorescent carbon dots. Mater Lett. 2024;358:135880.

18. Nandiyanto ABD, Oktiani R, Ragadhita R. How to read and interpret FTIR spectroscope of organic material. Indones J Sci Technol. 2019;4:97–118.

19. Lang Z, Pan J, Ma T, Feng S, Jin Q, Zhao M, et al. CuBi2O4/Bi2MoO6 heterojunction photocatalyst for degradation of tetracycline and rhodamine B: preparation, characterization, and mechanism study. J Mater Sci Mater Electron. 2024;35:803.

20. Acosta-Vergara J, Torres-Palma RA, Ávila-Torres Y. Solid state pelletizing for the synthesis of new Bi-doped strontium molybdate and its development as a photocatalytic precursor for Rhodamine B degradation. MethodsX. 2023;11:102258.

21. Zhou Y, Zhou Y, Chen A, Zhang J. Enhanced Photocatalytic Degradation of RhB by Plasmonic Type-II Ag/Ag2MoO4/BiOI Heterojunction. ChemistrySelect. 2022;7:e202202310.

22. Phuruangrat A, Keereesaensuk P-O, Karthik K, Dumrongrojthanath P, Ekthammathat N, Thongtem S, et al. Synthesis of Ag/Bi 2 MoO 6 nanocomposites using NaBH 4 as reducing agent for enhanced visible-light-driven photocatalysis of rhodamine B. J Inorg Organomet Polym Mater. 2020;30:322–9.

23. Gulpiya A, Su Z, Pan H. Hydrothermal synthesis of Ag2MoO4 with photocatalytic activity for rhodamine B degradation. J Aust Ceram Soc. 2021;57:91–6.

24. Saigl ZM. Various adsorbents for removal of rhodamine b dye: A review. Indones J Chem. 2021;21:1039–56.